

Topological Defects in Metal-Free Nanocarbon for Oxygen Electrocatalysis

Cheng Tang, Hao-Fan Wang, Xiang Chen, Bo-Quan Li, Ting-Zheng Hou, Bingsen Zhang, Qiang Zhang,* Maria-Magdalena Titirici,* and Fei Wei*

Modern life and society rely on energy more than ever. However, the current energy systems based on fossil fuels are confronted with grand challenges due to their finite resources and in particular the associated CO₂ emissions leading to climate change and environment destruction. Therefore, new and sustainable energy sources are necessary and, as a consequence, effective energy storage technologies need to be developed. Among several alternatives, regenerative fuel cells^[1–4] and rechargeable metal-air batteries^[5–7] have generated great expectations over the last decades. In spite of the substantial progress achieved in cathodes, anodes, and electrolyte, these prototypes suffer from poor energy efficiency due to the pronounced overvoltage and a low power capability, limited by the attainable current density.^[6] In both cases, oxygen electrodes with satisfactory electrocatalytic activities for oxygen reduction/evolution reactions (ORR/OER) are required for the regenerative operation and to accelerate these sluggish processes, thereby shrinking the potential gap between OER and ORR.^[8]

Enormous research efforts have been therefore directed towards the development of bifunctional ORR/OER catalysts. Among the most promising ORR/OER catalysts, perovskites,^[2,9] transition metal/metal oxides,^[3,10] and carbon-based materials and their composites^[11–18] have been explored. In particular, metal-free nanocarbon materials have been intensively investigated recently, due to their remarkable activity, high conductivity and flexibility, the tunable structure and surface chemistry, facile preparation, and economic viability. Heteroatom-doped (N, O, B, P, S, Si, etc.) carbon nanomaterials

are generally considered as excellent ORR catalysts under alkaline conditions.^[19–34] Additionally, some nitrogen-doped carbon materials have also shown considerable OER activities, but a limited durability.^[35–37]

The current theory behind the origin of electrocatalytic activity in heteroatom-doped carbon materials is based on the electroneutrality break and electron transfer induced by the heteroatom doping. Additionally, the surface functional groups, edge dangling bonds, and defective sites in nanocarbon materials also contribute to their electrocatalytic activity.^[12,17,21,38,39] Carbon nanostructures with higher edge exposure for the appropriate incorporation of nitrogen,^[40] especially within the distance of edge effect,^[12,17] are likely to be more active. Recently, it has been demonstrated that even dopant-free nanocarbon can deliver excellent ORR activity, which was attributed to the edge sites.^[41] However, up to now, the exact active sites in nanocarbon materials and their specific roles during ORR and OER remain elusive and controversial. Therefore, new insights into the origin and the role of nanocarbon active sites are very important for a better understanding and a rational design of metal-free carbon-based bifunctional catalysts for both ORR and OER.

In this contribution, we report a novel heteroatom-doped and edge-rich graphene material (nitrogen-doped graphene mesh, denoted as NGM hereinafter). This material was used as a model system to investigate the origin of electrocatalytic activity in nanocarbon catalysts both for ORR and OER. The NGM was obtained via the direct carbonization of sticky rice as carbon precursor, melamine as nitrogen source, and Mg(OH)₂ as template. This material exhibited a remarkable performance in both ORR and OER and it can be rated as one of the best metal-free bifunctional carbon catalysts ever reported. The effects of nitrogen doping, and edge defects were probed and first-principles simulations were carried out in order to elucidate the underlying mechanisms behind this remarkable performance. The results reveal the critical importance of edge and topological defects in the activity origin of metal-free nanocarbon materials for oxygen electrocatalysis. A nitrogen-free configuration with adjacent pentagon and heptagon carbon rings exhibits the lowest overpotential with 0.14 V for ORR and 0.21 V for OER.

The fabrication of NGM is illustrated in **Figure 1a**. A uniformly mixed ternary slurry was fabricated via in-situ precipitation of Mg(OH)₂ as a template precursor, gelatinized sticky rice as a carbon source and melamine as a nitrogen source, followed by natural drying, carbonization and purification (see details in the Supporting Information). Undoped graphene mesh (GM) was also prepared as a reference, under otherwise identical

C. Tang, H.-F. Wang, X. Chen, B.-Q. Li, T.-Z. Hou,
Prof. Q. Zhang, Prof. F. Wei
Beijing Key Laboratory of Green Chemical
Reaction Engineering and Technology
Department of Chemical Engineering
Tsinghua University
Beijing 100084, P. R. China
E-mail: zhang-qiang@mails.tsinghua.edu.cn;
wf-dce@tsinghua.edu.cn



C. Tang, Prof. Q. Zhang, Prof. M.-M. Titirici
Queen Mary University of London
School of Engineering and Materials Science
Mile End Road, E1 4NS London, UK
E-mail: m.m.titirici@qmul.ac.uk

Prof. B. Zhang
Shenyang National Laboratory for Materials Science
Institute of Metal Research
Chinese Academy of Sciences
Shenyang 110016, P. R. China

DOI: 10.1002/adma.201601406

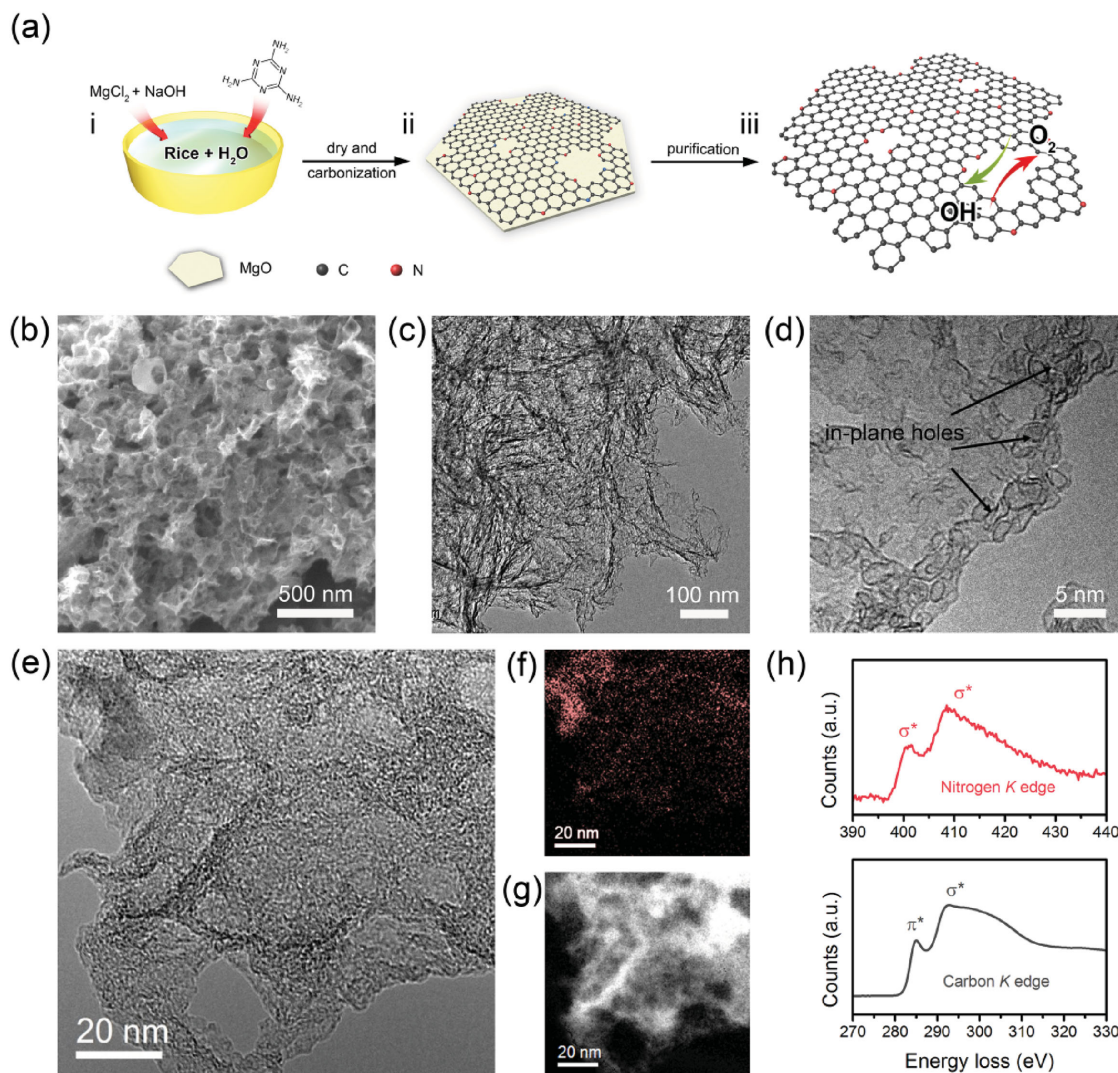


Figure 1. Synthesis and morphology characterization of NGM materials for bifunctional oxygen electrocatalysis. a) Schematic of the fabrication of NGM materials: i) ternary slurry in situ fabricated with templates, carbon source, and nitrogen source. ii) Casting of NGM on MgO templates at 950 °C. iii) NGM obtained after the removal of MgO templates and purification. b) SEM image showing the porous framework. c) TEM image showing the interconnected nanoplates of NGM. d) High-resolution TEM image of the porous graphene sheets. e) TEM image of the graphene layer, and corresponding f) N and g) C energy-filtered TEM images. h) Typical nitrogen and carbon K-edge EELS spectra of NGM.

conditions without the melamine addition. Both NGM and GM were employed as model electrocatalysts for ORR/OER.

The reason we choose gelatinized sticky rice as a carbon precursor is its uniform permeability and strong binding with inorganic templates. In fact, sticky rice has been already used as a binder for the Great Wall and other Asian traditional architectures. Herein, the as-obtained ternary precursors exhibit a range of sharp X-ray diffraction peaks, which can be mainly indexed to $\text{Mg}(\text{OH})_2$ and NaCl (Figure S1, Supporting Information). The scanning electron microscopy (SEM) images in Figure S2 (Supporting Information) show a hexagonal shape of $\text{Mg}(\text{OH})_2$ flakes with carbon/nitrogen uniformly wrapped. After the high temperature carbonization, the morphology of hexagonal flakes is maintained (Figure S3, Supporting Information). The yield of carbon herein is 4.8 ± 0.3 wt% of the

ternary precursors determined by thermogravimetric analysis (Figure S4, Supporting Information).

Ultrathin graphene flakes with a lateral size of ≈ 250 nm are obtained and self-assembled into a porous and hierarchical scaffold (Figure 1b–e and Figure S5, Supporting Information). Notably, the graphene flakes are dominantly few-layer type with nanosized holes all over the plane (Figure 1d and Figure S5c, Supporting Information). The energy-filtered transmission electron microscopy images (Figure 1f,g) indicate a homogeneous distribution of both C and N in the as-obtained NGM. As shown in Figure 1h, the characteristic π^* and σ^* transitions at ≈ 285.0 and 292.5 eV in the carbon K-edge spectrum suggest the sp^2 hybridization state of carbon in NGM.^[42] The peak at ≈ 401.5 eV in the nitrogen K-edge spectrum is assigned to the substitutional nitrogen configurations, such as the graphitic N,

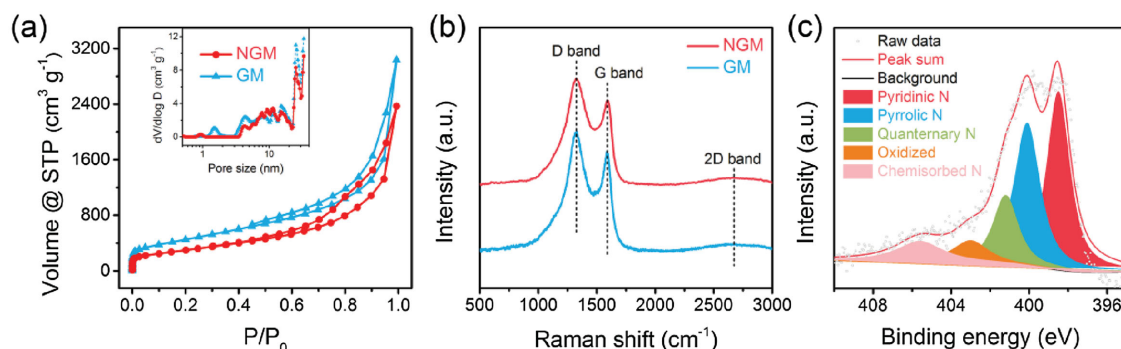


Figure 2. Structural characterization and properties of NGM materials. a) N_2 sorption isotherms of NGM and GM, inset figure illustrates the pore size distribution. b) Raman spectra of NGM and GM. c) The high-resolution N 1s XPS spectrum of NGM.

and the broad σ^* band around 408.5 eV is commonly ascribed to the pyridinic N conformation,^[43] which is recently demonstrated as the origin of active sites in nitrogen-doped carbon materials.^[44] This type of EELS feature indicates the dominantly sp^2 -hybridized N—C bonds in NGM.^[42]

The porosity of the as-fabricated NGM/GM was further evaluated by nitrogen adsorption (Figure 2a). The specific surface area is as high as $1655 \text{ m}^2 \text{ g}^{-1}$ for GM and $1100 \text{ m}^2 \text{ g}^{-1}$ for NGM. The pore size distribution dominantly exhibits a mesoporous structure (Table S1 in the Supporting Information, inset of Figure 2a), in good agreement with the TEM images. The porous MgO derived from $\text{Mg}(\text{OH})_2$ provides on one hand an efficient substrate to catalyse the decomposition of carbon/nitrogen sources, resulting in ultrathin graphene layers with a mesoporous framework and 3D conductive scaffold (NGM: $\approx 1.2 \text{ S cm}^{-1}$, GM: $\approx 5.8 \text{ S cm}^{-1}$).^[45–47] While on the other hand, the in-situ released water vapor and gas from the precursor decomposition and the random nucleation-growth behaviors from different sites of precursors on the substrate generate micro holes and edge sites. The resulting NaCl by-products can also serve as effective pore-forming agents (Figure S6, Supporting Information).^[48] The considerable amount of holes and edge defects in our material are further confirmed by the relatively high intensity of D bands in the Raman spectra (Figure 2b). The slightly higher I_D/I_G ratio of NGM with respect to GM (1.24 vs 1.11) is ascribed to the heteroatom-induced functionalities. X-ray photoelectron spectroscopy (XPS) survey spectra reveal a high N content of $\approx 7.60 \text{ at\%}$ for NGM, while only traces of heteroatom doping ($\approx 0.41 \text{ at\%}$) is recorded for GM. These nitrogen impurities originate from the natural sticky rice (Figure S7, Supporting Information). No signals of metal species are detected as there is no employment of metal precursors during the entire material fabrication. The N 1s spectra are deconvoluted into dominant pyridinic N, pyrrolic N, and quaternary N (Figure 2c and Figure S8, Table S2, Supporting Information), in good agreement with the EELS results. Such doping-derived sites and edge-rich holes are expected to act as active sites in the electrocatalytic reactions.^[12,17,40,44,49]

The electrocatalytic performance of NGM was first investigated on a rotating disk electrode (RDE) with a mass loading of $\approx 0.25 \text{ mg cm}^{-2}$. All potentials are calibrated to a reversible hydrogen electrode (RHE). As presented in Figure 3a, the iR -corrected linear scan voltammogram (LSV) profile in

O_2 -saturated solution reveals its superior ORR activity with a high current density approaching 7.5 mA cm^{-2} at 0 V vs RHE in 0.10 M KOH . The real ORR current density is obtained after subtracting the capacitive current (in N_2 -saturated electrolyte) from the O_2 -saturated current.^[21] It is notable that the NGM catalysts exhibit a very good activity in 0.10 M HClO_4 solution as well, with a high current density approaching 6.0 mA cm^{-2} . The much more negative onset potential (E_{onset}) suggests distinct active sites for ORR in different electrolytes, nevertheless, it is comparable with other metal-free catalysts in acidic conditions.^[44]

To further evaluate the ORR performances and pathways, rotating ring-disk electrode (RRDE) measurements were carried out. From the disk current density curves in Figure 3b, it can be observed that the E_{onset} and half-wave potential ($E_{1/2}$) of NGM ($E_{\text{onset}} \approx 0.89$, $E_{1/2} \approx 0.77$) are slightly lower than the commercial 20 wt\% Pt/C ($E_{\text{onset}} \approx 0.94$, $E_{1/2} \approx 0.80$), but a much higher diffusion-limiting current density of 6.41 mA cm^{-2} is obtained compared with Pt/C (4.97 mA cm^{-2}). In the case of GM, in spite of a much lower N content, a high current density about 5.72 mA cm^{-2} can be detected, while the overpotential is much larger than NGM ($E_{\text{onset}} \approx 0.83$, $E_{1/2} \approx 0.68$). If we normalize the current (at 0.47 V) with respect to the amount of N dopants, the specific current density of GM catalyst ($3.27 \text{ mA } \mu\text{g}_\text{N}^{-1}$) greatly surpasses that of NGM ($0.26 \text{ mA } \mu\text{g}_\text{N}^{-1}$), and even higher than the best reported result (NGSH, $2.60 \text{ mA } \mu\text{g}_\text{N}^{-1}$).^[14] NGM and GM share similar structures and porosity features, but deliver very different catalytic activities. Therefore, obviously the electrocatalytic activity does not only originate from the nitrogen dopants. To further elucidate this behavior, we prepared a nitrogen-doped graphene material (NG) with a similar N content of 7.48 at% but fewer in-plane holes and edges (Figure S9, Tables S1 and S2, Supporting Information). It was obtained by a hydrothermal treatment of graphene oxides as carbon precursors and urea as a nitrogen source. Interestingly, when an even higher N content is doped into the nanocarbon, the current density of NG is much lower than GM, strongly indicating the importance of the hole-induced edge sites in addition to the nitrogen dopants.

The electron transfer number per O_2 (n) is determined from the RRDE profiles (Figure 3c). NGM exhibits a similar n to Pt/C (around 3.8) over the whole potential range of 0.0–0.8 V, suggesting a dominant four-electron pathway of ORR. However,

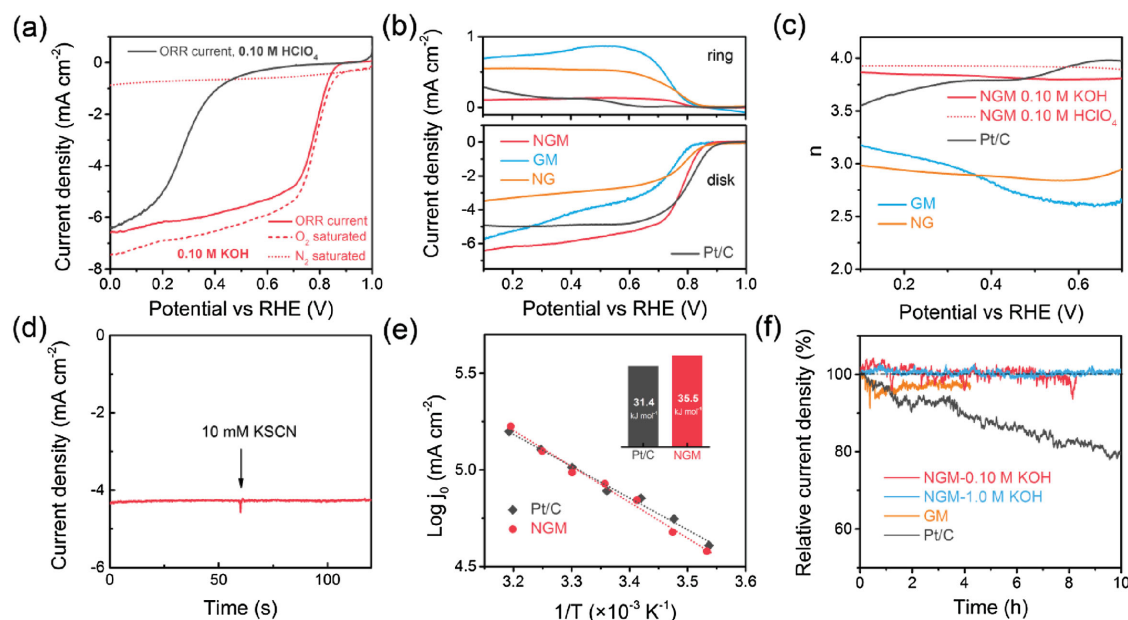


Figure 3. ORR performances of NGM materials. a) LSV curves of NGM obtained in O_2 or N_2 -saturated 0.10 M KOH or 0.10 M $HClO_4$ solutions. The difference between the current densities of O_2 or N_2 -saturated tests is assigned to the real ORR current (solid curves). All LSV profiles of ORR are obtained with such correction. b) The disk current densities (bottom) and ring current densities (top) recorded on an RRDE. c) Electron transfer number (n) derived from the LSV curves in RRDE measurements. d) Chronoamperometric response of NGM in O_2 -saturated 0.10 M KOH with the addition of KSCN (resulting in an electrolyte with 10×10^{-3} M KSCN). e) Arrhenius plots of Pt/C and NGM, showing the log of exchange current density j_0 versus the inverse temperature $1/T$, and the inset presents the calculated ORR apparent activation energies. f) ORR chronoamperometric responses at a constant potential of 0.60 V versus RHE for NGM, GM, and Pt/C. The rotating rate was 1600 rpm and a scan rate was 10 mV s^{-1} for all tests. All electrodes were prepared with the same mass loading of $\approx 0.25 \text{ mg cm}^{-2}$.

in the case of both GM and NG, n is much lower (2.5–3.2), revealing a different reaction pathway and clearly supporting the synergy between nitrogen doping and edge defects for NGM. Remarkably, the n of NGM obtained in 0.10 M $HClO_4$ is also approaching 4, even higher than that obtained in alkaline electrolytes. It further indicates superb activities of NGM in both acidic and alkaline conditions. To determine the origin of the superior activity, SCN^- ions were introduced into the electrolyte to strongly coordinate and poison iron-based catalytic sites if any (Figure 3d). Remarkably, no activity loss of the NGM electrode is observed after the addition of KSCN, corroborating the high intrinsic activity of this novel metal-free nanocarbon catalyst.

A noticeable increase (negatively) in the current densities with increasing temperature from 5 to 40 °C is observed for both Pt/C and NGM (Figure S10, Supporting Information), while the Tafel slopes decrease gradually (Figure S11, Supporting Information). This observation indicates that the ORR activity is mainly determined by the surface adsorption of oxygen species in a Frumkin-type behavior.^[50] Additionally, the apparent activation energy (E_a) for ORR is evaluated from the Arrhenius plots of the log of the exchange current density (j_0) versus the inverse of temperature (Figure 3e).^[50,51] It is revealed that the E_a of NGM is about 35.5 kJ mol^{-1} , and approaches the value of Pt/C (31.4 kJ mol^{-1}), directly verifying the high electrocatalytic activity of NGM.

Furthermore, both NGM and GM exhibit superior ORR durability as revealed by the chronoamperometric responses

(Figure 3f) at a constant potential of 0.60 V vs RHE. The ORR current retains as high as 98.5% of the initial value for NGM, even after 8.0 h tests in 0.10 M KOH. The LSV curve obtained after the long-period catalysis exhibits no change (Figure S12, Supporting Information). In contrast, Pt/C only retains 82.3% of its initial current. More remarkably, the NGM delivers a nearly constant current in 1.0 M KOH for more than 10 h, which further suggests the excellent stability of NGM catalysts for ORR (Figure 3f).

Both heteroatom dopants and edge-induced topological defects have been considered to redistribute the local electron density and provide a stronger affinity to the intermediates. This rationalizes the observation that NGM exhibits superior ORR activity and the ORR performance of GM is superior to NG despite of much lower nitrogen content. The more edge defects and edge-site doping in GM exist, the more effective active sites for ORR are generated. To further elucidate our experimental observations and confirm the activity origins, density functional theory (DFT) calculations were conducted based on the four-electron pathway mechanism for both ORR and OER (see details in the Supporting Information). Considering all the possible active sites derived from the nitrogen-doping, topological defects, and edge effects, several models are proposed systematically, including pyrrolic nitrogen (PR), pyridinic nitrogen (PN), quaternary nitrogen on the edge (Q), quaternary nitrogen in the bulk phase (QN), five-carbon ring (C5), seven-carbon ring (C7), and five-carbon ring adjacent to seven-carbon ring (C5+7), compared with the pristine graphene

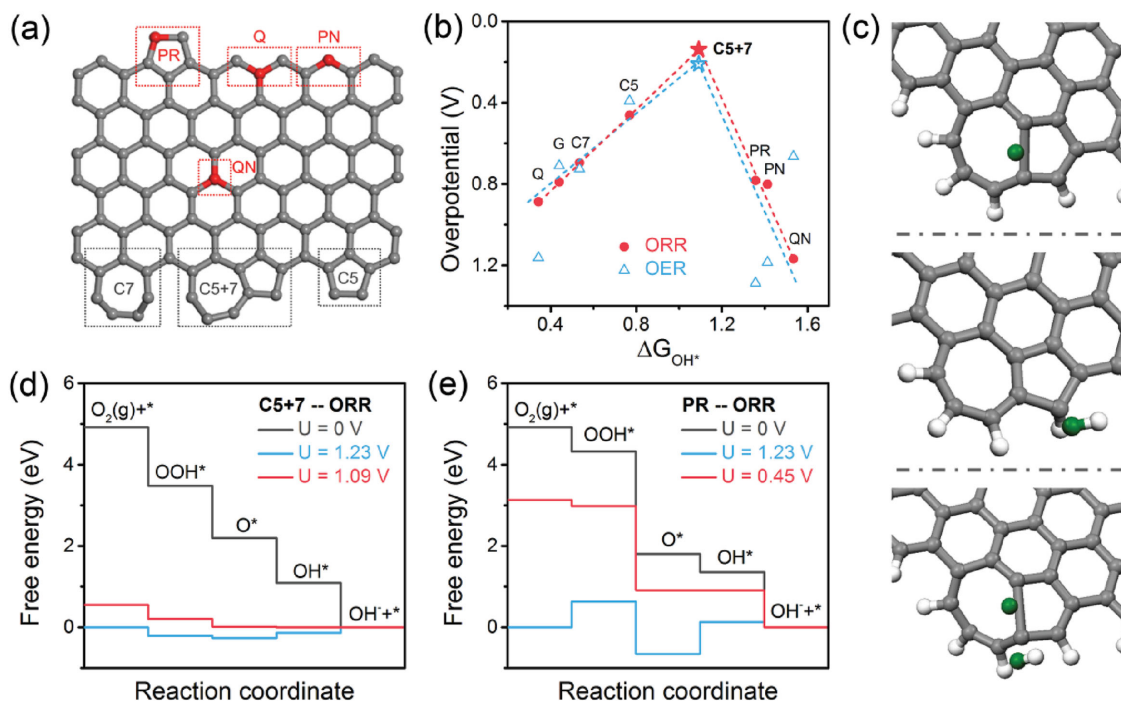


Figure 4. DFT calculations of ORR/OER activities for metal-free nanocarbon materials. a) A schematic graphene nanoribbon with different kinds of N-doping or topological defects. PR: pyrrolic nitrogen; PN: Pyridinic nitrogen; Q: quaternary nitrogen on the edge; QN: quaternary nitrogen in the bulk phase; C5: five-carbon ring; C7: seven-carbon ring; C5+7: five-carbon ring adjacent to seven-carbon ring. b) ORR and OER volcano plots of overpotential versus adsorption energy of OH^* , indicating the C5+7 as the optimal active site for both ORR and OER electrocatalysis. c) Optimized adsorption structure of C5+7 interacting with O, OH, and OOH species (from top to bottom). Calculated free energy diagrams of ORR at pH = 0 for the d) graphene nanoribbon with C5+7 defect and e) pyrrolic nitrogen dopant. The carbon, hydrogen, oxygen, and nitrogen elements are represented by gray, white, blue, and red, respectively in panels (a) and (c).

nanoribbon (G) as illustrated in **Figure 4a** and **Figure S13** (Supporting Information). The overpotential for each active site is calculated to serve as the vital figure-of-merit (**Figure 4b**, **Figure S14**, **Table S3**, Supporting Information).

Unexpectedly, for ORR catalysis, the N-doped moieties present a relatively higher overpotential compared to the pristine graphene nanoribbon, except for the PR configuration (**Figure S14a**, Supporting Information), which is different from Xia and co-workers' results.^[12] Among all nitrogen doping-induced sites, the sites near the edge exhibit a much lower overpotential, indicating the importance of edge effects, in consistency with previous calculations (**Figure S14b**, Supporting Information). However, the QN delivers an enhanced activity for OER compared with other doping-induced sites, suggesting that the favorable active sites for ORR and OER are distinct.^[11,12]

Topological defects are always induced upon heteroatom doping and they can also provide ORR electrocatalytic activity, for example, the nitrogen pair doped Stone-Wales defect.^[52] When these defects are considered, such as pentagon and heptagon carbon rings, the overpotential for ORR is remarkably decreased in our DFT calculation. The C5 can greatly reduce the overpotential by 0.33 V compared with the G. It is notable that the most active doped site PR for the N-containing configurations is also a five-atom ring. Furthermore, if the C5 adjoin C7 to form a curved configuration C5+7, the overpotential can

be further decreased to 0.14 V. Additionally, the OER overpotential of C5+7 is also as small as 0.21 V, much lower than other active sites (**Figure S14**, **Table S3**, Supporting Information).

A typical volcano plot is constructed for both ORR and OER, correlating the overpotential and descriptor (adsorption energy of OH^*), as shown in **Figure 4b**. The adsorption of OH species on Q sites is too weak, while the PN and QN sites enhance the binding overly, resulting in a high overpotential. Contrarily, the topological defects can regulate the binding energy towards an optimal value, rendering a superb bifunctionality for both ORR and OER at the peak of volcano plots (C5+7). The O and OOH species prefer to bind at the intersection of the five-carbon ring and seven-carbon rings as shown in **Figure 4c**. More interestingly, it is observed that the C5–C7 dipole in the C5+7 configuration could break the O–O bond in OOH species (greatly stretched O–O bonding length), leading to a facile reduction of oxygen (Movie 1, Supporting Information). The adjacent carbon rings with different electron densities generate spatial curvatures and are expected to form a permanent dipole moment. Such dipole moment is weaker than the one between nitrogen and carbon atoms. Therefore, a moderate adsorption and higher activity are achieved.

The free energy diagrams of ORR substeps on active site C5+7 are also predicted (**Figure 4d**). Desorption of OH^- is the last step to become downhill as the potential decreases. This is regarded to be the rate determining step. In contrast, the rate

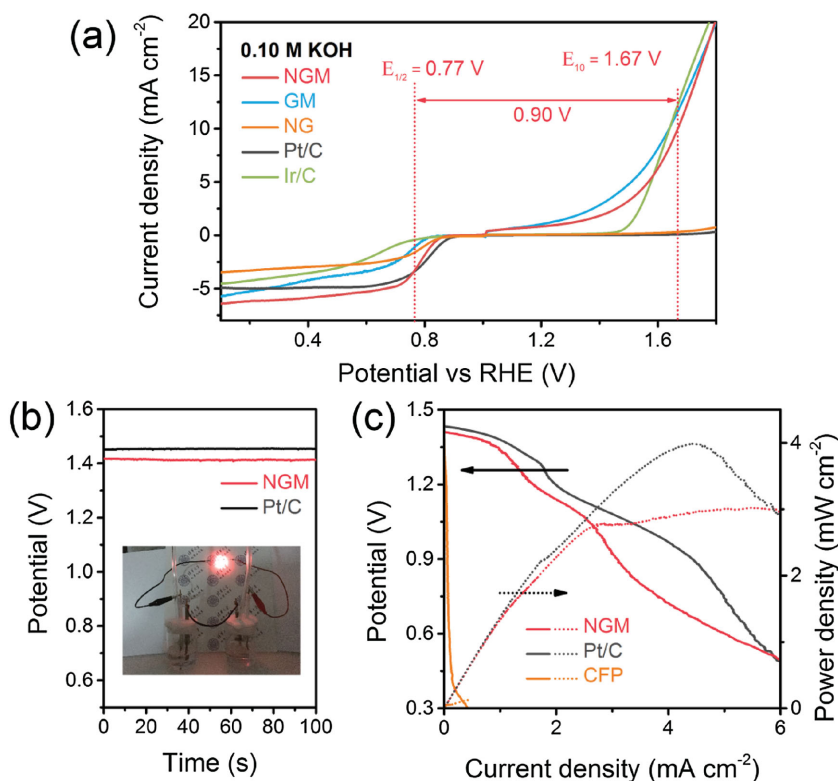


Figure 5. ORR/OER bifunctional activities and primary Zn-air battery performances. a) LSV curves of NGM, GM, NG, and commercial Pt/C, and Ir/C catalysts on an RDE in 0.10 M KOH, indicating the bifunctional activities toward both ORR and OER. b) Open circuit plots of the home-made primary Zn-air batteries with NGM, or Pt/C loading on CFP electrodes (mass loading of 0.8 mg cm⁻²) in O₂-saturated 6.0 M KOH electrolytes. The inset optical image shows an LED (≈ 2.2 V) lightened by two NGM-based Zn-air batteries in series. c) Polarization and power density curves of the primary Zn-air batteries. The scan rate was 5.0 mV s⁻¹.

determining step for PR is revealed to be the transformation of O* to OH* (Figure 4e). This further suggests the optimal adsorption of oxygen intermediates on C5+7 sites. This is for the first time we have demonstrated that an all-carbon topological defect can deliver an excellent activity for both ORR and OER. Topological defects with nitrogen incorporated are expected to further enhance the performances.^[52]

As demonstrated by the DFT results, both nitrogen-doped sites and topological defects near edge exhibit excellent OER activity as well. This is verified by the obvious anodic current above 1.2 V in LSV tests (Figure S15 in the Supporting Information, Figure 5a), which is assigned to the OER catalysis. Both NGM and GM exhibit greatly higher OER activity than Pt/C in terms of the onset potential and current density, and even comparable with the commercial 20 wt% Ir/C electrocatalysts. Unexpectedly, the OER performance of GM electrode is slightly better than its nitrogen-doped counterpart (NGM) and significantly surpasses the NG with a high nitrogen content. It can be rationalized by the distinct active sites for ORR and OER as illustrated by DFT.

Looking at both ORR and OER, the overall oxygen electrode activity is evaluated by the potential gap (ΔE) between the half-wave potential of ORR and potential required for an OER current density of 10 mA cm⁻².^[3,15,16] The NGM herein performs the best among all those metal-free bifunctional

catalysts reported recently with an oxygen electrode activity as low as 0.90 V,^[11,13–15] and even superior to some metal composites (Figure S16, Table S4, Supporting Information).^[3]

Furthermore, primary Zn-air batteries were constructed to investigate the practical application of as-obtained metal-free catalysts.^[53,54] The catalysts were uniformly loaded onto carbon fiber paper (CFP) with a loading of ≈ 0.8 mg cm⁻² as the cathode, and a Zn foil was paired in 6.0 M KOH as anode. A high open circuit voltage about 1.42 V is achieved for the NGM-based batteries (Figure 5b). As exemplified in the inset of Figure 5b, a light-emitting diodes (LED) can be lightened by two Zn-air batteries in series. Figure 5c presents the polarization and power density curves for NGM, compared with Pt/C and the pristine CFP based Zn-air batteries. The NGM electrode exhibits a current density of ≈ 6.0 mA cm⁻² and a peak power density of ≈ 3.0 mW cm⁻², comparable to those of a Pt/C electrode and better than some previous works.^[54] This prototype demonstration without any optimization proves the potential application of such metal-free nanocarbon catalysts for Zn-air batteries.

In summary, the reaction pathway of ORR/OER has been probed through both theoretical calculations and experimentally electrochemical evaluation using a unique nitrogen-doped and edge-rich 3D graphene model system obtained via the carbonization

of natural rice. The in-situ fabricated MgO catalytic templates are critical for effective graphitization of solid carbon/nitrogen sources and the generation of abundant in-plane holes. The best bifunctional activities for both ORR and OER among all the reported metal-free catalysts has been achieved on NGM electrocatalyst. The overpotential gap is as low as 0.90 V, with an excellent ORR performance superior to Pt/C in terms of both activity and stability, and a remarkable OER activity comparable with Ir/C. The ORR activity in acidic conditions is also considerable. Both edge effects and topological defects are more favorable for both ORR and OER, instead of the nitrogen-doped sites. A nitrogen-free configuration with adjacent pentagon and heptagon carbon rings exhibits the lowest overpotential for both ORR and OER at the peak of volcano plots. A prototype Zn-air battery based on the NGM catalysts is constructed. This work provides fresh insights into the origins of oxygen electrocatalytic activity for metal-free nanocarbon electrocatalysts. Specifically, the importance of topological defects, in addition to the doping-induced sites in the heteroatom-doped nanocarbon materials is elucidated towards promising ORR/OER catalysis. The impact of this work is that it will inspire the understanding of underlying mechanisms, and facilitate the targeted design and fabrication of advanced metal-free carbocatalysts, aiming at optimal performances for a wide range of electrocatalytic applications.

Supporting Information

Supporting Information is available from the Wiley Online Library or from the author.

Acknowledgements

C.T., H.-F.W., and X.C. contributed equally to this work. This work was supported by funding from the Natural Scientific Foundation of China (No. 21306102, 21422604, and 21561130151), Tsinghua University Initiative Scientific Research Program (20161080166), and National Basic Research Program of China (2015CB932500). B.Z. thanks the financial support provided by the National Natural Science Foundation of China (91545119) and the Youth Innovation Promotion Association CAS (2015152). Q.Z. and M.M.T. thank the Royal Society for the award of a Newton Advanced Fellowship (Ref: NA140249).

Received: March 12, 2016

Revised: April 12, 2016

Published online: May 11, 2016

- [1] M. K. Debe, *Nature* **2012**, *486*, 43.
- [2] J. Suntivich, H. A. Gasteiger, N. Yabuuchi, H. Nakanishi, J. B. Goodenough, Y. Shao-Horn, *Nat. Chem.* **2011**, *3*, 546.
- [3] Y. Gorlin, T. F. Jaramillo, *J. Am. Chem. Soc.* **2010**, *132*, 13612.
- [4] Y. Y. Liang, Y. G. Li, H. L. Wang, J. G. Zhou, J. Wang, T. Regier, H. J. Dai, *Nat. Mater.* **2011**, *10*, 780.
- [5] F. Y. Cheng, J. Chen, *Chem. Soc. Rev.* **2012**, *41*, 2172.
- [6] L. Grande, E. Paillard, J. Hassoun, J. B. Park, Y. J. Lee, Y. K. Sun, S. Passerini, B. Scrosati, *Adv. Mater.* **2015**, *27*, 784.
- [7] Y. G. Li, H. J. Dai, *Chem. Soc. Rev.* **2014**, *43*, 5257.
- [8] P. G. Bruce, S. A. Freunberger, L. J. Hardwick, J. M. Tarascon, *Nat. Mater.* **2012**, *11*, 19.
- [9] J. I. Jung, H. Y. Jeong, J. S. Lee, M. G. Kim, J. Cho, *Angew. Chem. Int. Ed.* **2014**, *53*, 4582.
- [10] K. L. Pickrahn, S. W. Park, Y. Gorlin, H.-B.-R. Lee, T. F. Jaramillo, S. F. Bent, *Adv. Energy Mater.* **2012**, *2*, 1269.
- [11] J. Zhang, Z. Zhao, Z. Xia, L. Dai, *Nat. Nanotechnol.* **2015**, *10*, 444.
- [12] M. T. Li, L. P. Zhang, Q. Xu, J. B. Niu, Z. H. Xia, *J. Catal.* **2014**, *314*, 66.
- [13] G. L. Tian, Q. Zhang, B. S. Zhang, Y. G. Jin, J. Q. Huang, D. S. Su, F. Wei, *Adv. Funct. Mater.* **2014**, *24*, 5956.
- [14] G. L. Tian, M. Q. Zhao, D. S. Yu, X. Y. Kong, J. Q. Huang, Q. Zhang, F. Wei, *Small* **2014**, *10*, 2251.
- [15] T. Y. Ma, J. Ran, S. Dai, M. Jaroniec, S. Z. Qiao, *Angew. Chem. Int. Ed.* **2015**, *54*, 4646.
- [16] Y. Zhao, K. Kamiya, K. Hashimoto, S. Nakanishi, *J. Phys. Chem. C* **2015**, *119*, 2583.
- [17] L. B. Ma, X. P. Shen, G. X. Zhu, Z. Y. Ji, H. Zhou, *Carbon* **2014**, *77*, 255.
- [18] S. Dou, L. Tao, J. Huo, S. Wang, L. Dai, *Energy Environ. Sci.* **2016**, *9*, 1320.
- [19] L. J. Yang, S. J. Jiang, Y. Zhao, L. Zhu, S. Chen, X. Z. Wang, Q. Wu, J. Ma, Y. W. Ma, Z. Hu, *Angew. Chem. Int. Ed.* **2011**, *50*, 7132.
- [20] L. F. Lai, J. R. Potts, D. Zhan, L. Wang, C. K. Poh, C. H. Tang, H. Gong, Z. X. Shen, L. Y. Jianyi, R. S. Ruoff, *Energy Environ. Sci.* **2012**, *5*, 7936.
- [21] D. W. Wang, D. S. Su, *Energy Environ. Sci.* **2014**, *7*, 576.
- [22] D. S. Geng, Y. Chen, Y. G. Chen, Y. L. Li, R. Y. Li, X. L. Sun, S. Y. Ye, S. Knights, *Energy Environ. Sci.* **2011**, *4*, 760.
- [23] K. P. Gong, F. Du, Z. H. Xia, M. Durstock, L. M. Dai, *Science* **2009**, *323*, 760.
- [24] Z. W. Liu, X. Fu, M. Li, F. Wang, Q. D. Wang, G. J. Kang, F. Peng, *J. Mater. Chem. A* **2015**, *3*, 3289.
- [25] Z. Yang, Z. Yao, G. F. Li, G. Y. Fang, H. G. Nie, Z. Liu, X. M. Zhou, X. Chen, S. M. Huang, *ACS Nano* **2012**, *6*, 205.
- [26] C. Z. Zhang, N. Mahmood, H. Yin, F. Liu, Y. L. Hou, *Adv. Mater.* **2013**, *25*, 4932.
- [27] L. M. Dai, Y. H. Xue, L. T. Qu, H. J. Choi, J. B. Baek, *Chem. Rev.* **2015**, *115*, 4823.
- [28] J. Duan, S. Chen, M. T. Jaroniec, S. Z. Qiao, *ACS Catal.* **2015**, *5*, 5207.
- [29] D. S. Yu, L. Wei, W. C. Jiang, H. Wang, B. Sun, Q. Zhang, K. L. Goh, R. M. Si, Y. Chen, *Nanoscale* **2013**, *5*, 3457.
- [30] W. Wei, H. W. Liang, K. Parvez, X. D. Zhuang, X. L. Feng, K. Mullen, *Angew. Chem. Int. Ed.* **2014**, *53*, 1570.
- [31] L. T. Qu, Y. Liu, J. B. Baek, L. M. Dai, *ACS Nano* **2010**, *4*, 1321.
- [32] S. B. Yang, L. J. Zhi, K. Tang, X. L. Feng, J. Maier, K. Mullen, *Adv. Funct. Mater.* **2012**, *22*, 3634.
- [33] S. Y. Wang, L. P. Zhang, Z. H. Xia, A. Roy, D. W. Chang, J. B. Baek, L. M. Dai, *Angew. Chem. Int. Ed.* **2012**, *51*, 4209.
- [34] H. Jin, H. Huang, Y. He, X. Feng, S. Wang, L. Dai, J. Wang, *J. Am. Chem. Soc.* **2015**, *137*, 7588.
- [35] T. Y. Ma, S. Dai, M. Jaroniec, S. Z. Qiao, *Angew. Chem. Int. Ed.* **2014**, *53*, 7281.
- [36] L. Wang, Y. Huang, C. Li, J. J. Chen, X. Sun, *Synth. Met.* **2014**, *198*, 300.
- [37] Y. Zhao, R. Nakamura, K. Kamiya, S. Nakanishi, K. Hashimoto, *Nat. Commun.* **2013**, *4*, 2390.
- [38] Y. Jiao, Y. Zheng, M. Jaroniec, S. Z. Qiao, *J. Am. Chem. Soc.* **2014**, *136*, 4394.
- [39] D. S. Su, S. Perathoner, G. Centi, *Chem. Rev.* **2013**, *113*, 5782.
- [40] E. J. Biddinger, U. S. Ozkan, *J. Phys. Chem. C* **2010**, *114*, 15306.
- [41] L. Tao, Q. Wang, S. Dou, Z. Ma, J. Huo, S. Wang, L. Dai, *Chem. Commun.* **2016**, *52*, 2764.
- [42] Y. M. Lin, X. L. Pan, W. Qi, B. S. Zhang, D. S. Su, *J. Mater. Chem. A* **2014**, *2*, 12475.
- [43] R. Arenal, K. March, C. P. Ewels, X. Rocquefelte, M. Kociak, A. Loiseau, O. Stephan, *Nano Lett.* **2014**, *14*, 5509.
- [44] D. Guo, R. Shibuya, C. Akiba, S. Saji, T. Kondo, J. Nakamura, *Science* **2016**, *351*, 361.
- [45] C. Tang, B. Q. Li, Q. Zhang, L. Zhu, H. F. Wang, J. L. Shi, F. Wei, *Adv. Funct. Mater.* **2016**, *26*, 577.
- [46] C. Tang, H. S. Wang, H. F. Wang, Q. Zhang, G. L. Tian, J. Q. Nie, F. Wei, *Adv. Mater.* **2015**, *27*, 4516.
- [47] A. Scott, A. Dianat, F. Borrnert, A. Bachmatiuk, S. S. Zhang, J. H. Warner, E. Borowiak-Palen, M. Knupfer, B. Buchner, G. Cuniberti, M. H. Rummeli, *Appl. Phys. Lett.* **2011**, *98*, 073110.
- [48] J. Qin, C. N. He, N. Q. Zhao, Z. Y. Wang, C. S. Shi, E. Z. Liu, J. J. Li, *ACS Nano* **2014**, *8*, 1728.
- [49] W. J. Yuan, Y. Zhou, Y. R. Li, C. Li, H. L. Peng, J. Zhang, Z. F. Liu, L. M. Dai, G. Q. Shi, *Sci. Rep.* **2013**, *3*, 2248.
- [50] T. J. Schmidt, V. Stamenkovic, J. P. N. Ross, N. M. Markovic, *Phys. Chem. Chem. Phys.* **2003**, *5*, 400.
- [51] A. Parthasarathy, S. Srinivasan, A. J. Appleby, C. R. Martin, *J. Electrochem. Soc.* **1992**, *139*, 2530.
- [52] G. L. Chai, Z. F. Hou, D. J. Shu, T. Ikeda, K. Terakura, *J. Am. Chem. Soc.* **2014**, *136*, 13629.
- [53] Y. G. Li, M. Gong, Y. Y. Liang, J. Feng, J. E. Kim, H. L. Wang, G. S. Hong, B. Zhang, H. J. Dai, *Nat. Commun.* **2013**, *4*, 1805.
- [54] S. Chen, J. Duan, P. Bian, Y. Tang, R. Zheng, S.-Z. Qiao, *Adv. Energy Mater.* **2015**, *5*, 1500936.